HHS Public Access

Author manuscript

MAGMA. Author manuscript; available in PMC 2017 June 01.

Published in final edited form as:

MAGMA. 2016 June ; 29(3): 359–370. doi:10.1007/s10334-015-0509-0.

Ultrashort Echo Time and Zero Echo Time MRI at 7T

Peder E. Z. Larson, PhD[1,2,*], **Misung Han, PhD**[1], **Roland Krug, PhD**[1], **Angela Jakary**[1], **Sarah J. Nelson, PhD**[1,2], **Daniel B. Vigneron, PhD**[1,2], **Roland G. Henry, PhD**[1,3], **Graeme McKinnon, PhD**[4], and **Douglas A. C. Kelley, PhD**[4]

[1]Department of Radiology and Biomedical Imaging, University of California - San Francisco, San Francisco, California, USA

[2]UC Berkeley-UCSF Graduate Program in Bioengineering, University of California, Berkeley and University of California, San Francisco, California, USA

[3]Department of Neurology, University of California - San Francisco, San Francisco, California, USA

[4]GE Healthcare, Waukesha, Wisconsin, USA

Abstract

Object—Zero echo time (ZTE) and ultrashort echo time (UTE) pulse sequences for MRI offer unique advantages of being able to detect signal from rapidly decaying short-T2 tissue components. In this paper, we applied 3D zero echo time (ZTE) and ultrashort echo time (UTE) pulse sequences at 7T to assess differences between these methods.

Materials and Methods—We matched the ZTE and UTE pulse sequences closely in terms of readout trajectories and image contrast. Our ZTE used the Water- and fat-suppressed solid-state proton projection imaging (WASPI) method to fill the center of k-space. Images from healthy volunteers obtained at 7T were compared qualitatively as well as with SNR and CNR measurements for various ultrashort, short, and long-T2 tissues.

[*]Address correspondence to: Peder Larson, Byers Hall, Rm 102C, 1700 4th St, San Francisco, CA 94158, ; Email: peder.larson@ucsf.edu

Author Contributions

Larson - Protocol/project development, Data collection or management, Data analysis
Han - Protocol/project development, Data collection or management
Krug - Protocol/project development
Jakary - Data collection or management
Nelson - Protocol/project development
Vigneron - Protocol/project development
Henry - Protocol/project development, Data collection or management
McKinnon - Protocol/project development
Kelley - Protocol/project development, Data collection or management, Data analysis

Compliance with Ethical Standards

Disclosure of potential conflicts of interest We have the following potential conflicts of interest: this work was supported in part by Research Funding from GE Healthcare (PI: Dr. Nelson). Drs. McKinnon and Kelley are employees of GE Healthcare.

Research involving Human Participants and/or Animals All procedures performed in studies involving human participants were in accordance with the ethical standards of the institutional research committee and with the 1964 Helsinki declaration and its later amendments or comparable ethical standards.

Informed consent Informed consent was obtained from all individual participants included in the study.

Results—We measured nearly identical contrast-to-noise and signal-to-noise ratios (CNR/SNR) in similar scan times between the two approaches for ultrashort, short, and long-T2 components in the brain, knee and ankle. In our protocol, we observed gradient fidelity artifacts in UTE, and our chosen flip angle and readout also resulted as well as shading artifacts in ZTE due to inadvertent spatial selectivity. These can be corrected by advanced reconstruction methods or with different chosen protocol parameters.

Conclusion—The applied ZTE and UTE pulse sequences achieved similar contrast and SNR efficiency for volumetric imaging of ultrashort-T2 components. Several key differences are that ZTE is limited to volumetric imaging but has substantially reduced acoustic noise levels during the scan. Meanwhile, UTE has higher acoustic noise levels and greater sensitivity to gradient fidelity, but offers more flexibility in image contrast and volume selection.

Keywords

Magnetic Resonance Imaging; Neuroimaging; Musculoskeletal System

Introduction

Tissues and tissue components with ultrashort-T2 relaxation times of less than approximately 1 ms cannot be reliably detected by conventional MRI pulse sequences due to limitations on the minimum achievable echo time (TE). Zero echo time (ZTE) and ultrashort echo time (UTE) pulse sequences use specialized acquisition and reconstruction techniques to enable detection of ultrashort-T2 components in vivo. These sequences allow for direct visualization of tendons ($T_2^* \approx 1\,\mathrm{ms}$) ([1–7]), cortical bone ($T_2^* \approx 0.4\,\mathrm{ms}$) ([8–16]), and lung parenchyma ($T_2^* \approx 0.5-3\,\mathrm{ms}$) ([17–22]), as well as components in myelin ($T_2^* \approx 0.1-0.4\,\mathrm{ms}$ ([23–25])) and ligaments ([26]) (up to 80% fraction of $T_2^* \approx 1\,\mathrm{ms}$ ([27])).

UTE pulse sequences rely on beginning data acquisition as soon as possible after completion of the RF pulses. The readout gradients are turned on at the beginning of data acquisition, leading to a center-out k-space trajectory. Typically radial trajectories are used, although other center-out trajectories such as spirals ([28]), twisted projections ([29]), or cones ([30]) are also feasible. UTE can be acquired in either 2D or 3D mode, with 2D requiring the use of half-pulse excitations ([31]).

ZTE pulse sequences also rely on beginning data acquisition as soon as possible after completion of the RF pulses. However, unlike UTE, the readout gradients are turned on prior to the RF pulse ([32, 33]). Therefore the center of k-space is crossed at echo time of zero. A similar strategy is also used in the Sweep imaging with Fourier transformation (SWIFT) method ([34]). However, due to switching of hardware from transmit to receive mode, the center of k-space is not sampled, and data is acquired starting at some minimum k-space radius. Strategies to fill in the center of k-space include using algebraic reconstruction ([35,36]), single-point imaging (Pointwise encoding time reduction with radial acquisition, PETRA) ([37]), and reduced amplitude readouts (Solid-state magnetic resonance imaging, SMRI/Water- and fat-suppressed solid-state proton projection imaging, WASPI) ([9]). Typically radial trajectories are used in ZTE for the outer portion of k-space. Having the readout gradients on during the RF excitation pulse can potentially introduce some spatial-

selectivity, and for this reason the RF flip angles and readout bandwidths are typically limited to ensure that this selectivity does not affect the imaging volume. This also means ZTE can only be used for 3D imaging. A recently touted advantage of ZTE is its substantially reduced ambient noise levels (used in “silent” MRI), improving patient comfort.

In this paper, we applied 3D ZTE and UTE pulse sequences in vivo at 7T. This was motivated by the increasing interest in these techniques and the purpose of this work was to assess any differences (SNR, contrast, artifacts) when the pulse sequences were very similar. To this end, the image contrast, k-space trajectories, and image reconstruction were closely matched in an attempt to highlight any fundamental differences between the two pulse sequences. For ZTE, the WASPI method was used to fill the center of k-space ([9]). We performed these studies at ultrahigh field (7T) for several reasons: the increased polarization is advantageous for ultrashort-T2 imaging because these tissue components often have low proton density and their ultra-fast relaxation rate limits the data acquisition time, both contributing to overall low SNR; and the increased B0 and B1 inhomogeneities at 7T will accentuate any differences between the sequences due to these effects. Any artifacts due to B0 or B1 inhomogeneities we have observed in this study will be reduced when using lower field strengths such as 3T. We compared the SNR and contrast in several different tissues in the brain, knee and ankle to reveal any differences between the sequences (SNR efficiency, detection of ultrashort-T2 tissue components, image contrast).

A major limitation of this study was that we did not explore all differences between UTE and ZTE, such as flip angle restrictions, multi-echo readouts, volume selection capability, and gradient calibrations, so an extensive qualitative comparison of these differences is presented in the Discussion. Another limitation was that there were some pulse sequence differences, including switching times, delay times, and spatial selection, that impacted our results. These differences are described in detail in the Methods and their anticipated impact is described in the Discussion.

Materials and Methods

Figure 1 shows the UTE and ZTE pulse sequences used in this study. We attempted to use identical parameters as much as possible in both pulse sequences. Identical parameters included the RF pulse (12–20 μs hard pulse, 4° flip), resolution, FOV, readout bandwidth and duration. The readout window is shown by the “DAQ” in Fig. 1a, where UTE begins with the ramp up of the gradient and ends at the end of the plateau, while ZTE begins after the transmit/receive (T/R) switching delay (T/R delay). All gradients were designed to reach the same k-space radius at the end of the readout. The timing of the radial k-space trajectory and maximum gradient amplitudes are slightly different even with identical readout bandwidths and durations because for UTE the readout window and sampling includes the ramp up of the gradient, meanwhile for ZTE the readout window does not include the center of k-space and has no gradient ramps.

Both pulse sequences used periodically applied fat-suppression pulses (4 ms, 1 kHz bandwidth, 100° flip) for improved ultrashort-T2 component contrast in the ankle, knee and

skull. In the brain studies, both sequences also included an inversion recovery (IR) preparation scheme using an adiabatic inversion pulse (HS2 pulse shape ([38]), 20 ms, 1.6 kHz bandwidth) for additional contrast ([25,39]). The IR preparation pulse was applied every 384 projections with an inversion delay time, TI = 600ms, and a recovery time, TD = 1s. Key pulse sequence parameters are listed in Table 1.

For both pulse sequences, 3D isotropic FOV and resolution radial trajectories were used. These were oversampled in the radial direction by approximately a factor of two relative to the Nyquist sampling requirement. These were undersampled angularly by an overall factor of π relative to the Nyquist sampling requirement at the end of the projections. The angular undersampling results in relatively diffuse, noise-like artifacts, and thus this degree of undersampling can typically be applied without noticeable artifacts. For ZTE, the center of k-space was filled in by acquiring an additional set of low-frequency projections with lower gradient strengths as in the WASPI method ([9]). The gradients were reduced by a factor of 8 compared to the rest of the data and the angular density was reduced to support the same FOV, meaning $8^2 = 64$ times fewer lines were acquired in the additional low-frequency acquisition. The first 32 samples of this acquisition were combined with the high-frequency data in the gridding reconstruction to fill in the center of k-space. A linear-weighting was applied to the last 8 of these low-frequency samples and the first 2 high-frequency samples to reduce ringing artifacts. All coils were combined with a sum-of-squares for UTE and ZTE.

There were a few differences between the UTE and ZTE sequences used, primarily arising from the fact that the UTE sequence was developed in-house at UCSF while the ZTE sequence was developed within GE Healthcare. The ZTE pulse sequence was optimize to have a shorter minimum transmit/receive switching time of 8 μs, compared to 70 μs in the UTE sequence. The ZTE scan times were also increased due to some additional delay time that was automatically added by the pulse sequence program based on expected SAR calculations, although ultimately this extra time was not necessary to stay within FDA limits. Finally, the ZTE excitation pulses introduced some slice selection artifact, resulting from the gradient being applied during excitation. With the chosen RF duration and readout gradient amplitudes, the full-width half-maximum (FWHM) slice thicknesses of the hard pulse excitation was 10.8 cm (brain), 15.1 cm (ankle), and 10.4 (knee), with nulls (i.e. no excitation) at ± the FWHM thickness. This artifact can be corrected to some extent in the reconstruction ([40]), but we did not apply these corrections in this study.

Phantom experiments were performed using a resolution phantom with varying sizes of signal voids. We used the same parameters as the in vivo brain experiments listed below, except without the adiabatic IR preparation.

Seven healthy volunteers were imaged on a 7 T MRI system (GE Healthcare, Waukesha, Wisconsin, USA) equipped with 50 mT/m maximum amplitude and 200 mT/m/ms maximum slew rate gradients. Informed consent was obtained before scans under an Institutional Review Board (IRB) approved protocol. For the head and ankle studies, a head-only quadrature coil was used to transmit and a 32-channel phased-array head coil (Nova Medical, Wilmington, MA) was used to receive signal. For the ankle studies, the subjects lay

supine with one foot located in the head coil. The anterior part of the phased-array coil was shifted off to fit the foot in a relaxed position in the coil, as done in ([7]). This resulted in the lower leg being positioned nearly parallel to B0, minimizing magic angle effects for tendons running superior/inferior. For knee studies, we used a knee-only 2 channel transmitter with an optimized static phase offset between the two channels to generate circular polarization along with a 28-channel phased-array knee coil (Quality Electrodynamics/QED, Mayfield Village, Ohio, USA) to receive signal. The scanner and these RF coils were able to achieve 8 μs transmit-receive switching times with the standard MRI system hardware.

We also scanned 6 patients previously diagnosed with multiple sclerosis with either our UTE (1 patient) or ZTE (5 patients) brain protocol. The standard imaging protocol included an IR-prepared spoiled gradient recalled (SPGR) acquired with TE = 2.3 ms, TR = 6.2 ms, TI = 600 ms, 8° flip, and 1 mm isotropic resolution, which we used for a qualitative comparison.

SNR and CNR comparisons were performed by drawing regions of interest (ROIs) in various tissues. Mean signals were measured within the tissue of interest. Measuring noise is challenging due to diffuse, noise-like artifacts from radial undersampling that will appear across the image as well as amplitude variations due to the coil geometry and combination. Thus we chose to measure noise from the standard deviation in a ROI with homogeneously-appearing tissue. The noise ROI was chosen to be nearby to the tissue of interest in order to minimize the effects of coil geometry and sum-of-squares noise distortion. One limitation of the SNR and CNR measurements is that the diffuse, noise-like artifacts from the angular undersampling will create a background signal that will contribute to the noise measurement. However, these artifacts should be very similar between ZTE and UTE because the same angular undersampling was used. These measurements will also be confounded by the aforementioned ZTE slice selection artifact (resulting from the gradient being applied during excitation), particularly near the edges of the FOV. ZTE and UTE data were compared using a Student’s T-test, paired within each volunteer.

Results

We performed phantom experiments in order to assess the image quality, resolution capabilities and off-resonance sensitivity of UTE and ZTE sequences (Fig. 2). The sequences had nearly identical radial readout trajectories, which we expected to have an identical resolution and similar phase accumulation due to off-resonance. However, the ZTE sequence used additional extra low-resolution projections to fill the center of k-space that could have an impact on image quality, resolution, and artifacts. Our phantom results showed that the resolution capabilities of both approaches were comparable. Phase accumulation during the radial readouts due to off-resonance resulted in an isotropic blurring and ringing artifact in both pulse sequences. This can be seen in all the resolution phantom compartments: in the larger compartments, the edges are blurred out; and in the smaller compartments there was even signal enhancement at the larger off-resonance frequencies. There are some very subtle differences: in the 200 Hz off-resonance the larger compartments have a sharper ringing artifact with ZTE that is slightly smoother with UTE.

We performed in vivo imaging studies in the brain, ankle, and knee to assess the detection of ultrashort-T2 signals, image quality, and artifact behavior. In vivo brain imaging results shown in Fig. 3 demonstrate comparable image contrast within brain tissue, where an identical IR preparation provided contrast between gray and white matter and they also showed similar vascular enhancement. However, ZTE had slightly SNR in the white matter, as quantified later, which has been shown to contain ultrashort-T2 components ($T_2^* \approx 0.1-0.4\,\mathrm{ms}$ ([23–25])). Both sequences comparably detected ultrashort-T2 signals from cortical bone in the skull ($T_2^* \approx 0.4\,\mathrm{ms}$, dashed orange arrows). Typically, ZTE had increased signal from ultrashort-T2 components in the RF coil and foam padding (wide green arrows). ZTE suffered from increased apparent blurring around the skull and skin (dashed yellow arrows), as well as shading and signal dropout artifacts at the edges of the FOV (thin red arrows). The shading and signal dropout artifacts are a result of slice selection effects from the RF pulse being applied during the readout gradients, which are particularly noticeable at the most anterior and posterior portions of the head in the axial image (top row) as well as inferiorly in the neck in the sagittal image. In our ZTE brain protocol, the full-width half-maximum (FWHM) slice thickness of the hard pulse excitation was 10.8 cm, with nulls (i.e. no excitation) at ±10.8 cm, which explains these artifacts. Methods for correcting for the slice selection effects in ZTE are included in the Discussion.

In vivo ankle imaging results shown in Fig. 4 also demonstrated comparable image contrast, with 0.7 mm isotropic resolution in less than 5 minutes of scan time. With both ZTE and UTE we observed a fascicular pattern in the Achilles tendon ($T_2^* \approx 1\,\mathrm{ms}$, dashed orange arrows), where stripes of higher signal represented endotenon, whereas those of lower signal represented fascicles, as we had previously observed in 18 minute scan times with UTE at 7T ([7]). Similar image contrast was achieved through periodic application of fat suppression pulses, and we also observed numerous other tendons in the ankle (dashed yellow arrows). The use of fat suppression was crucial for image contrast because the fat off-resonance artifacts will create artificial structure and blurring at fat-water interfaces, demonstrated by our previous 7T UTE studies in the ankle ([7]). In the ankle, no shading and signal dropout artifacts were observed in ZTE since the FWHM slice thickness of the hard pulse excitation was 15.1 cm, which was large enough to cover most of the ankle in all directions. ZTE had increased signal from ultrashort-T2 components in the RF coil and foam padding (wide green arrows). We observed some failures of the fat-suppression pulses, particularly in the heel (thin red arrows), where large susceptibility-induced frequency shifts are present.

In vivo knee imaging results shown in Fig. 5 also demonstrated comparable image contrast for the numerous connective tissues in the knee, including ligaments, cartilage, and the meniscus at 0.8 mm isotropic resolution in less than 5 minutes of scan time with both ZTE and UTE. As in the brain, we did observe some shading artifacts with ZTE (thin red arrows), particularly at the edges of the FOV, due to the slice selection effects of ZTE. For this ZTE protocol, the FWHM slice thickness of the hard pulse excitation was 10.4 cm, with nulls at ±10.4 cm, which explains the shading artifacts in the superior/inferior direction. We also observed eddy current distortion artifacts with UTE (thin red arrows). This can be corrected by several methods, including using gradient measurements ([41]) and pre-compensation or post-processing corrections.

Sample raw data for the different sequences and protocols is shown in Fig. 6 to demonstrate the differences in timing and filling the k-space center between the UTE and ZTE sequences. In general, there is a strong correspondence between the methods. Some varying signal fluctuations are seen at the beginning of the acquisitions, likely due to stabilization of the receiver hardware and filters. The overall signal intensities were similar. The remaining deviations in the data could be due to off-resonance accumulation, which will be different across k-space in the low-resolution ZTE acquisitions, and spatial selectivity of the RF pulses modulating the ZTE raw data.

We compared SNR values for various tissues as well as CNR between selected tissues in Fig. 7 across all studies. We chose ultrashort-T2 tissues (ankle tendons, cortical bone in the skull, patellar ligament) as well as tissues with substantial longer T2 components. White matter ([25]), meniscus and cartilage may also have substantial ultrashort-T2 components in addition to the typically observed short and long-T2 components. The SNR difference were not statistically significant between UTE and ZTE ($p > 0.05$) except in white matter, where the ZTE SNR was higher with statistical significance ($p < 0.05$). The CNR differences were not statistically significant between UTE and ZTE ($p > 0.05$).

Data acquired using IR UTE and ZTE in two multiple sclerosis patients is shown in Fig. 8. These provided good contrast for suspicious demyelinated lesions, similar to the IR SPGR images. The foam padding and skull are clearly visualized in the UTE and ZTE images only. Comparable ZTE results were obtained in all 5 patients scanned with ZTE.

Discussion

Overall, in this study we observed very similar performance in several regards between UTE and ZTE pulse sequences for brain, ankle and knee imaging at 7T. Specifically, artifacts due to off-resonance and radial undersampling were similar as was the image contrast and SNR of most tissues, including tendons and cortical bone that have sub-millisecond T2 relaxation times. Both sequences supported using fat suppression and inversion recovery pulses for contrast generation. The B0 inhomogeneity at 7T resulted in some failure of the fat-suppression pulses, which would be less likely at lower field strengths (e.g. 3T). The B1 inhomogeneity somewhat surprisingly did not have much impact on image quality and contrast, possibly due to the low-flip angle, short TR acquisition as well as the adiabatic IR pulse used in the head studies. However, we observed some different artifacts between ZTE and UTE, including shading/signal dropoff and eddy current distortions. Our general observations comparing ZTE and UTE are described in Table 2.

In tendons and cortical bone that have 0.5–1 millisecond T2 relaxation times, we found the SNR was similar between UTE and ZTE. However, ZTE had higher signal from the foam pads and components of the RF coils (e.g. plastics), which most likely have even shorter-T2 values than the tissues used for the SNR measurements. (For this reason it is desirable to use padding and RF coil materials with lower proton densities and/or very rapid relaxation times ([42]) as well as specialized coil placement and shielding configurations ([43]).) We also observed higher SNR with ZTE in white matter. This could be a result of ultrashort-T2 white matter components ($T_2^* \approx 10-100\,\mu s$ ([23],[24])) that were better detected with ZTE.

We believe the increased ZTE SNR from foam pads, coil components, and white matter is largely due to the different switching times between excitation and acquisition in the UTE and ZTE - the minimum switching delays were 70 μs for the UTE sequence but 8 μs for the ZTE sequence that had been further optimized with respect to delay. This is based on our point spread function (PSF) simulation of the UTE and ZTE pulse sequences used in this study shown in Fig. 9. The loss of signal for shorter T2 values with both sequences is a result of the transmit/receive delay and T2 decay during the readout. (The musculoskeletal protocol total readout duration (1.28 ms) was longer as compared to the brain protocol (0.768 ms) leading to more signal decay during the readout ([44]), which explains why it had a relatively lower expected ultrashort-T2 signal.) For the brain protocol, the ZTE sequence had predicted 33% and 8.1% greater signal compared to the UTE sequence for T2 values of 0.3 and 1 ms, respectively. This is consistent with the increased foam padding and white matter SNR in the ZTE brain images. But we also did not observe statistically significant differences in SNR for cortical bone in the skull ($T_2^* \approx 0.4\,\mathrm{ms}$). This could be explained by spatial selectivity at the edges of the FOV for ZTE (discussed below) reducing the cortical bone SNR. This effect could also have reduced the gray matter SNR as well, because it also is towards the edges of the FOV.

For the ankle and knee protocols, ZTE had predicted 33% and 7.8% greater signal compared to the UTE for T2 values of 0.3 and 1 ms, respectively. This is consistent with the increased foam padding signal in the ZTE ankle images. We did not observe statistically significant differences in SNR for tendons ($T_2^* \approx 1\,\mathrm{ms}$) in our studies, and expected signal difference was lower for this T2 regime. However, this difference does not conclusively favor ZTE for ultrashort-T2 imaging, as our UTE implementation was not optimized to achieve the fastest possible transmit-receive switching. With an optimized UTE implementation the expected signal levels between ZTE and UTE are nearly identical in our PSF simulation (“UTE (T/R delay = 8 μs)” in Fig. 9).

Our phantom results showed some very subtle differences in the off-resonance response. We were unable to identify the cause of this via point spread function (PSF) simulations. It may arise from the WASPI central k-space filling technique imparting some k-space filtering.

In our ZTE acquisitions, we observed shading and signal drop off artifacts due to the varying spatial selectivity of the RF pulse being applied during the readout gradients. In other words, the RF excitation is behaving as a slice-selective pulse, causing signal loss, although the direction of the slice selection is changing for different readouts, resulting in a combination of signal loss and shading artifact ([40]). We could have avoided this by decreasing the readout bandwidth (decreasing readout gradient strengths) or shortening the RF pulse (increasing RF excitation bandwidth), but both of these options limit the steady-state contrast achievable. In particular, decreasing the readout bandwidth will allow for more ultrashort-T2 signal decay during the readout, blurring these tissues of interest, and shortening the RF pulse limits the achievable flip angles. Our RF pulse durations were set by the peak B1 of the coils and the desired flip angle (4-degrees). While this ZTE artifact is a limitation of our comparison study, but also highlights how ZTE sequences have more restrictions on the flip angles and readout bandwidths compared to UTE. Correcting for this artifact is an active area of research. Recent work has addressed this using reconstruction

techniques that account for the spatial selectivity ([40]) and shaped excitation pulses to increase the uniformly excited FOV ([45]).

In our UTE knee acquisitions, we observed distortion artifacts due to sources of gradient infidelity such as eddy currents and other timing delays. These were not observed when using the head coil, suggesting it was due to eddy currents in the knee coil. We applied simple x, y and z axis gradient delay corrections, although these did not completely eliminate the artifacts. This can be corrected by numerous methods, including using gradient measurements ([41]) and pre-compensation or post-processing corrections. Sensitivity to gradient infidelity is inherent in UTE due to the use of ramp sampling ([46]). One advantage of ZTE, on the other hand, is that it requires very little gradient ramping (resulting in a very quiet scan) and therefore is quite robust to sources of gradient infidelity.

In general, UTE currently offers more image contrast and imaging volume flexibility than ZTE, which could be a significant advantage for clinical applications. (These differences were not demonstrated in this study, as we purposefully matched the contrast and volumes between the methods for a more straight forward comparison.) For contrast, UTE sequences can use a large range of excitation flip angles, RF pulse durations, and readout gradients compared to ZTE sequences that are limited by the shading and signal drop-off artifact in ZTE. UTE can also include slab selective excitation pulses to limit the 3D FOV or be applied as a 2D method by using half-pulse excitations ([31]) (although these pulses are very sensitive to gradient infidelity), both of which are not possible with ZTE. UTE sequences also often include multiple echo time readouts to generate ultrashort-T2 contrast, and have also been applied with more efficient k-space trajectories, such as spirals ([28]), twisted projections ([29]), or cones ([30]). ZTE is also potentially compatible with multiple echo times and slightly modified versions of more efficient trajectories, but it loses its advantages of robustness to gradient infidelity and acoustically quiet scanning.

In terms of the scan time, ZTE can achieve shorter TRs because of the minimal gradient switching requirements. However, when using WASPI ([9]), or single-point imaging (PETRA) ([37]) to fill the center of k-space, some extra acquisitions are required for ZTE compared to UTE. With fast enough switching times, the center of k-space can be filled using algebraic reconstruction ([35], [36]) without any extra acquisitions, resulting in shorter scan times compared to UTE. (This ZTE approach has a different ultrashort-T2 component response and off-resonance phase accumulation compared to the WASPI method used in this study.) In our study, the ZTE scan time was also increased due to some additional delay time that was automatically added by the pulse sequence program based on expected SAR calculations, although ultimately this was not necessary to stay within FDA limits.

Conclusion

We found that ZTE and UTE pulse sequences can achieve very similar contrast and SNR efficiency for volumetric imaging of ultrashort-T2 components. This was performed at 7T to take advantage of the increased polarization and also to accentuate any pulse sequence differences due to B0 and B1 inhomogeneity, although we observed negligible differences in image quality between ZTE and UTE due to these inhomogeneities. The contrast in both

sequences benefited significantly from using fat suppression and inversion recovery RF preparation pulses, enabling clear visualization of ultrashort-T2 components such as the cortical bone in the skull as well as tendons with SNRs > 20 in less than 5 minutes. In our implementation, we observed shading artifacts in ZTE due to spatial selectivity as well as gradient fidelity artifacts in UTE, although methods exist to correct for both of these artifacts. In general, UTE has more flexibility in image contrast and imaging volume selection but has a greater sensitivity to gradient fidelity, while ZTE is limited to volumetric imaging but has substantially reduced noise levels during the scan.

Acknowledgments

We would like to thank the volunteers who participated in this study, as well as Kim Butts Pauly, Rob Peters and Michael Carl for helpful comments and discussions on the methods and images. This work was supported by the National Institutes of Health (NIH) grant S10-RR026845, the NIH-NCRR UCSF-CTSI (Grant Number UL1 RR024131), GE Healthcare, National Multiple Sclerosis Society Pilot Grant (Grant Number PP3360), and UCSF Department of Radiology and Biomedical Imaging Seed Grants.

References

1. Gold, GE.; Wren, TAL.; Nayak, KS. In vivo short echo time imaging of Achilles tendon. Proceedings of the 9th Annual Meeting of ISMRM; Glasgow. 2001. p. 244
2. Robson MD, Benjamin M, Gishen P, Bydder GM. Magnetic resonance imaging of the Achilles tendon using ultrashort TE (UTE) pulse sequences. Clin Radiol. 2004; 59:727–735. [PubMed: 15262548]
3. Filho GH, Du J, Pak BC, Statum S, Znamorowski R, Haghighi P, Bydder G, Chung CB. Quantitative characterization of the achilles tendon in cadaveric specimens: T1 and R2* measurements using ultrashort-TE MRI at 3 T. AJR Am J Roentgenol. 2009; 192:W117–24. [PubMed: 19234239]
4. Grosse U, Syha R, Martirosian P, Wuerslin C, Horger M, Grözinger G, Schick F, Springer F. Ultrashort echo time MR imaging with off-resonance saturation for characterization of pathologically altered achilles tendons at 3 T. Magn Reson Med. 2013; 70:184–92. [PubMed: 22851408]
5. Juras V, Zbyn S, Pressl C, Valkovic L, Szomolanyi P, Frollo I, Trattnig S. Regional variations of T2* in healthy and pathologic achilles tendon in vivo at 7 tesla: preliminary results. Magn Reson Med. 2012; 68:1607–13. [PubMed: 22851221]
6. Wright P, Jellus V, McGonagle D, Robson M, Ridgeway J, Hodgson R. Comparison of two ultrashort echo time sequences for the quantification of T(1) within phantom and human achilles tendon at 3 T. Magn Reson Med. 2012; 68:1279–84. [PubMed: 22246857]
7. Han M, Larson PEZ, Liu J, Krug R. Depiction of achilles tendon microstructure in vivo using high-resolution 3-dimensional ultrashort echo-time magnetic resonance imaging at 7 T. Invest Radiol. 2014; 49:339–45. [PubMed: 24500089]
8. Reichert IL, Robson MD, Gatehouse PD, He T, Chappell KE, Holmes J, Girgis S, Bydder GM. Magnetic resonance imaging of cortical bone with ultrashort TE pulse sequences. Magn Reson Imaging. 2005; 23:611–618. [PubMed: 16051035]
9. Wu Y, Dai G, Ackerman JL, Hrovat MI, Glimcher MJ, Snyder BD, Nazarian A, Chesler DA. Water- and fat-suppressed proton projection MRI (WASPI) of rat femur bone. Magn Reson Med. 2007; 57:554–67. [PubMed: 17326184]
10. Techawiboonwong A, Song HK, Leonard MB, Wehrli FW. Cortical bone water: in vivo quantification with ultrashort echo-time MR imaging. Radiology. 2008; 248:824–33. [PubMed: 18632530]
11. Horch RA, Nyman JS, Gochberg DF, Dortch RD, Does MD. Characterization of 1H NMR signal in human cortical bone for magnetic resonance imaging. Magn Reson Med. 2010; 64:680–7. [PubMed: 20806375]

12. Du J, Carl M, Bydder M, Takahashi A, Chung CB, Bydder GM. Qualitative and quantitative ultrashort echo time (UTE) imaging of cortical bone. J Magn Reson. 2010; 207:304–11. [PubMed: 20980179]
13. Keereman V, Fierens Y, Broux T, DeDeene Y, Lonneux M, Vandenberghe S. MRI-based attenuation correction for PET/MRI using ultrashort echo time sequences. J Nucl Med. 2010; 51:812–8. [PubMed: 20439508]
14. Krug R, Larson PEZ, Wang C, Burghardt AJ, Kelley DAC, Link TM, Zhang X, Vigneron DB, Majumdar S. Ultrashort echo time MRI of cortical bone at 7 tesla field strength: a feasibility study. J Magn Reson Imaging. 2011; 34:691–5. [PubMed: 21769960]
15. Weiger M, Stampanoni M, Pruessmann KP. Direct depiction of bone microstructure using MRI with zero echo time. Bone. 2013; 54:44–7. [PubMed: 23356986]
16. Wiesinger F, Sacolick LI, Menini A, Kaushik SS, Ahn S, VeitHaibach P, Delso G, Shanbhag DD. Zero TE MR bone imaging in the head. Magn Reson Med. 2015; doi: 10.1002/mrm.25545
17. Bergin CJ, Pauly JM, Macovski A. Lung parenchyma: projection reconstruction MR imaging. Radiology. 1991; 179:777–781. [PubMed: 2027991]
18. Kuethe DO, Caprihan A, Fukushima E, Waggoner RA. Imaging lungs using inert fluorinated gases. Magn Reson Med. 1998; 39:85–8. [PubMed: 9438441]
19. Stock KW, Chen Q, Hatabu H, Edelman RR. Magnetic resonance T2* measurements of the normal human lung in vivo with ultra-short echo times. Magn Reson Imaging. 1999; 17:997–1000. [PubMed: 10463650]
20. Johnson KM, Fain SB, Schiebler ML, Nagle S. Optimized 3D ultrashort echo time pulmonary MRI. Magn Reson Med. 2013; 70:1241–50. [PubMed: 23213020]
21. Weiger M, Wu M, Wurnig MC, Kenkel D, Jungraithmayr W, Boss A, Pruessmann KP. Rapid and robust pulmonary proton ZTE imaging in the mouse. NMR Biomed. 2014; 27:1129–34. [PubMed: 25066371]
22. Gibiino F, Sacolick L, Menini A, Landini L, Wiesinger F. Free-breathing, zero-te MR lung imaging. Magn Reson Mater Phy. 2015; 28:207–15.
23. Horch RA, Gore JC, Does MD. Origins of the ultrashort-T(2) (1)H NMR signals in myelinated nerve: A direct measure of myelin content? Magn Reson Med. 2011; 66:24–31. [PubMed: 21574183]
24. Wilhelm MJ, Ong HH, Wehrli SL, Li C, Tsai PH, Hackney DB, Wehrli FW. Direct magnetic resonance detection of myelin and prospects for quantitative imaging of myelin density. Proc Natl Acad Sci U S A. 2012; 109:9605–10. [PubMed: 22628562]
25. Du J, Sheth V, He Q, Carl M, Chen J, CoreyBloom J, Bydder GM. Measurement of T1 of the ultrashort T2* components in white matter of the brain at 3T. PLoS One. 2014; 9:e103296. [PubMed: 25093859]
26. Rahmer J, Börnert P, Dries SPM. Assessment of anterior cruciate ligament reconstruction using 3D ultrashort echo-time MR imaging. J Magn Reson Imaging. 2009; 29:443–8. [PubMed: 19161200]
27. Du J, Diaz E, Carl M, Bae W, Chung CB, Bydder GM. Ultrashort echo time imaging with bicomponent analysis. Magn Reson Med. 2012; 67:645–9. [PubMed: 22034242]
28. Du J, Bydder M, Takahashi AM, Chung CB. Two-dimensional ultrashort echo time imaging using a spiral trajectory. Magn Reson Imaging. 2008; 26:304–12. [PubMed: 18096346]
29. Boada FE, Gillen JS, Shen GX, Chang SY, Thulborn KR. Fast three dimensional sodium imaging. Magn Reson Med. 1997; 37:706–715. [PubMed: 9126944]
30. Gurney PT, Hargreaves BA, Nishimura DG. Design and analysis of a practical 3D cones trajectory. Magn Reson Med. 2006; 55:575–582. [PubMed: 16450366]
31. Pauly, JM.; Conolly, SM.; Nishimura, DG.; Macovski, A. Slice-selective excitation for very short T_2 species. Proc., SMRM, 8th Annual Meeting; Amsterdam. August 1989; p. 28
32. Hafner S. Fast imaging in liquids and solids with the back-projection low angle shot (BLAST) technique. Magn Reson Imaging. 1994; 12:1047–51. [PubMed: 7997092]
33. Madio DP, Lowe IJ. Ultra-fast imaging using low flip angles and FIDs. Magn Reson Med. 1995; 34:525–9. [PubMed: 8524019]

34. Idiyatullin D, Corum C, Park JY, Garwood M. Fast and quiet MRI using a swept radiofrequency. J Magn Reson. 2006; 181:342–9. [PubMed: 16782371]
35. Weiger M, Hennel F, Pruessmann KP. Sweep MRI with algebraic reconstruction. Magn Reson Med. 2010; 64:1685–95. [PubMed: 20949600]
36. Weiger M, Brunner DO, Dietrich BE, Müller CF, Pruessmann KP. ZTE imaging in humans. Magn Reson Med. 2013; 70:328–32. [PubMed: 23776142]
37. Grodzki DM, Jakob PM, Heismann B. Ultrashort echo time imaging using pointwise encoding time reduction with radial acquisition (PETRA). Magn Reson Med. 2012; 67:510–8. [PubMed: 21721039]
38. Tannus A, Garwood M. Improved performance of frequency-swept pulses using offset-independent adiabaticity. J Magn Reson A. 1996; 120:133–137.
39. Li C, Magland JF, Rad HS, Song HK, Wehrli FW. Comparison of optimized soft-tissue suppression schemes for ultrashort echo time MRI. Magn Reson Med. 2012; 68:680–689. [PubMed: 22161636]
40. Grodzki DM, Jakob PM, Heismann B. Correcting slice selectivity in hard pulse sequences. J Magn Reson. 2012; 214:61–7. [PubMed: 22047992]
41. Duyn JH, Yang Y, Frank JA, van der Veen JW. Simple correction method for k-space trajectory deviations in MRI. J Magn Reson. 1998; 132:150–3. [PubMed: 9615415]
42. Springer F, Martirosian P, Schwenzer NF, Szimtenings M, Kreisler P, Claussen CD, Schick F. Three-dimensional ultrashort echo time imaging of solid polymers on a 3-tesla whole-body MRI scanner. Invest Radiol. 2008; 43:802–8. [PubMed: 18923260]
43. Horch RA, Wilkens K, Gochberg DF, Does MD. RF coil considerations for short-T2 MRI. Magn Reson Med. 2010; 64:1652–7. [PubMed: 20665825]
44. Rahmer J, Börnert P, Groen J, Bos C. Three-dimensional radial ultrashort echo-time imaging with T2 adapted sampling. Magn Reson Med. 2006; 55:1075–82. [PubMed: 16538604]
45. Schieban K, Weiger M, Hennel F, Boss A, Pruessmann KP. ZTE imaging with enhanced flip angle using modulated excitation. Magn Reson Med. 2014
46. Tyler DJ, Robson MD, Henkelman RM, Young IR, Bydder GM. Magnetic resonance imaging with ultrashort TE (UTE) pulse sequences: technical considerations. J Magn Reson Imaging. 2007; 25:279–89. [PubMed: 17260388]

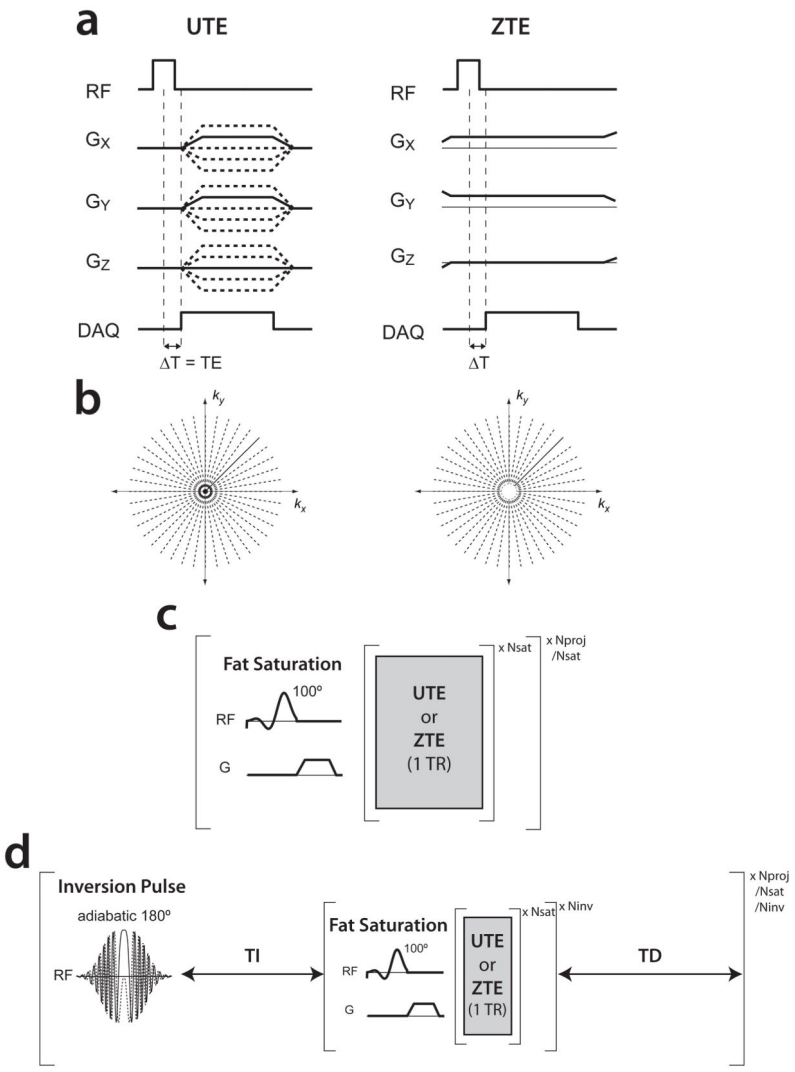

Figure 1.

(a,b) A single TR of the 3D UTE and ZTE pulse sequences used, with the corresponding k-space coverage. The missing central k-space in ZTE was filled using low-resolution projections ([9]). Sequence timing diagram for the (c) knee, ankle, and (d) brain studies including periodically applied fat suppression and inversion recovery pulses.

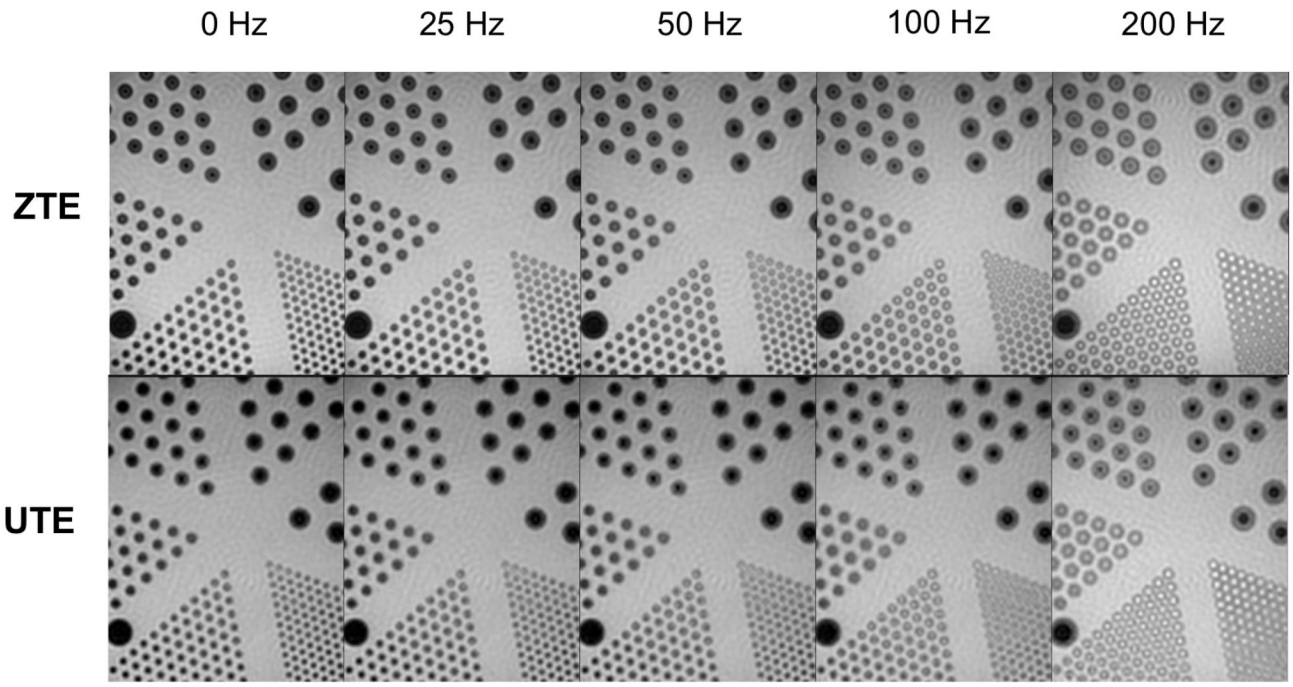

Figure 2.

Resolution phantom experiments acquired with different center frequencies. These demonstrate the off-resonance sensitivity of both techniques, where phase accumulation during the radial readouts results in an isotropic blurring and ringing artifact. This can be seen by the increased signal in the center of the resolution phantom circles, which should be void of signal. These artifacts are nearly identical between ZTE and UTE.

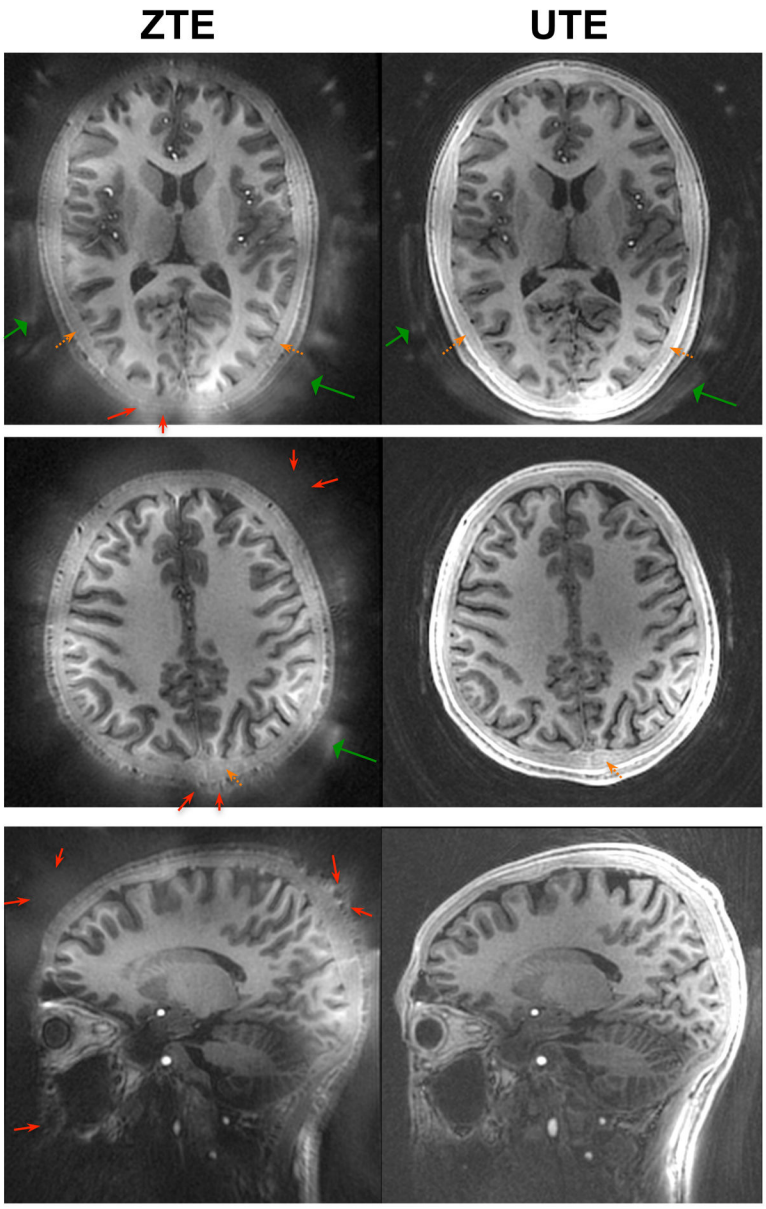

Figure 3.

In vivo brain imaging results in a healthy volunteer at 1.1 mm isotropic resolution with fat-suppression pulses and IR preparation. UTE and ZTE demonstrated similar gray/white matter contrast. Both detected signal from the cortical bone in the skull (dashed orange arrows). Signal was also seen from the RF coil and foam padding (wide green arrows), with typically more signal in the ZTE images. In this study, ZTE suffered from some shading and signal dropout artifacts near the edges of the FOV (thin red arrows), although this can be alleviated through improved sequence and reconstruction methods as discussed in the text.

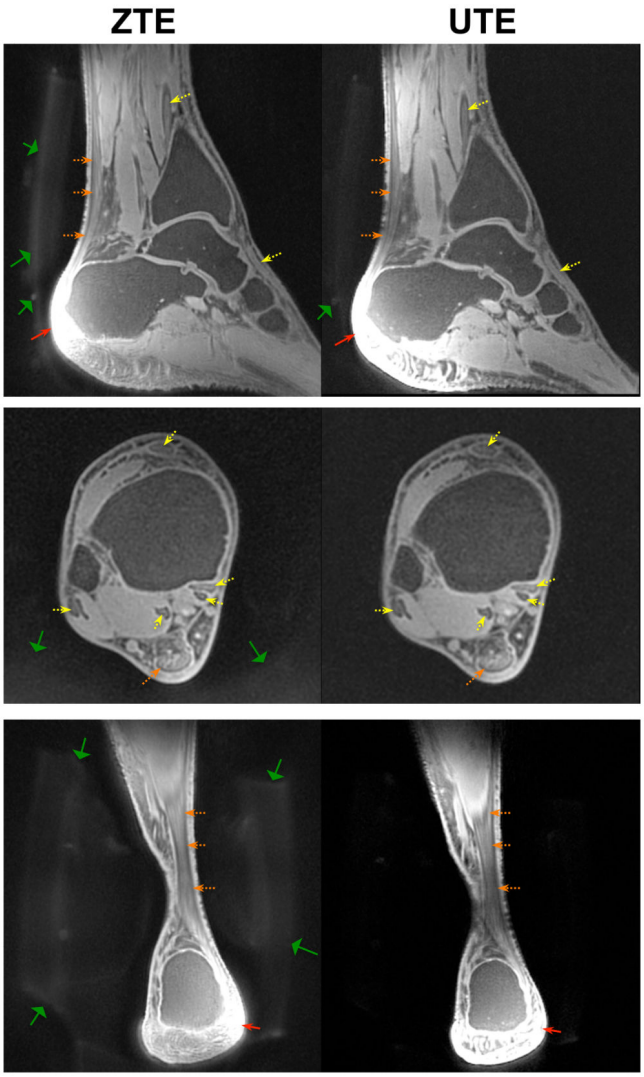

Figure 4.

In vivo ankle imaging results in a healthy volunteer at 0.7 mm isotropic resolution with fat-suppression pulses. UTE and ZTE demonstrated similar contrast for ultrashort-T2 components in tendons (dashed yellow arrows). In particular, both showed a fascicular structure in the Achilles tendon (dashed orange arrows). ZTE showed increased signal from foam padding (wide green arrows). Some failure of the fat suppression pulses was observed, particularly in the heel (thin red arrows).

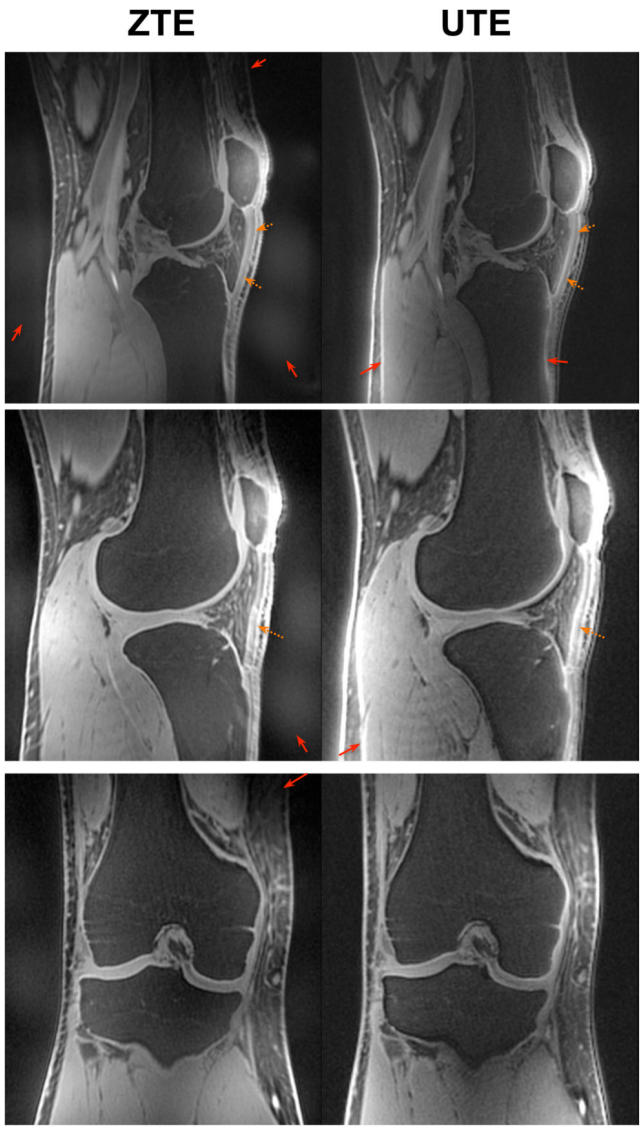

Figure 5.

In vivo knee imaging results in a healthy volunteer at 0.8 mm isotropic resolution with fat-suppression pulses. UTE and ZTE demonstrated similar contrast for connective tissues such as the patellar ligament (dashed orange arrows) as well as for other ligaments, cartilage, and the meniscus. Similarly to the brain results (Fig. 3), ZTE suffered from some shading and signal dropout artifacts (thin red arrows). Methods for correcting these artifacts are included in the Discussion.

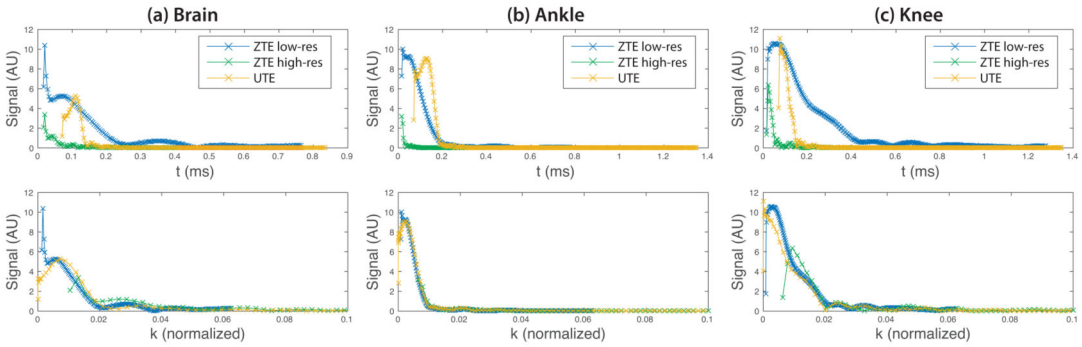

Figure 6.

Sample raw data from UTE and ZTE acquisitions in the (a) brain, (b) ankle, and (c) knee. The k-space data is normalized to pixel values, such that the maximum extent in k-space is ±0.5 1/pixel, and only up to a radius of 0.1 is shown. The ZTE data includes the low-resolution projection data required to fill in the center of k-space for the WASPI technique up to a radius of $k \approx 0.01$ 1/pixel.

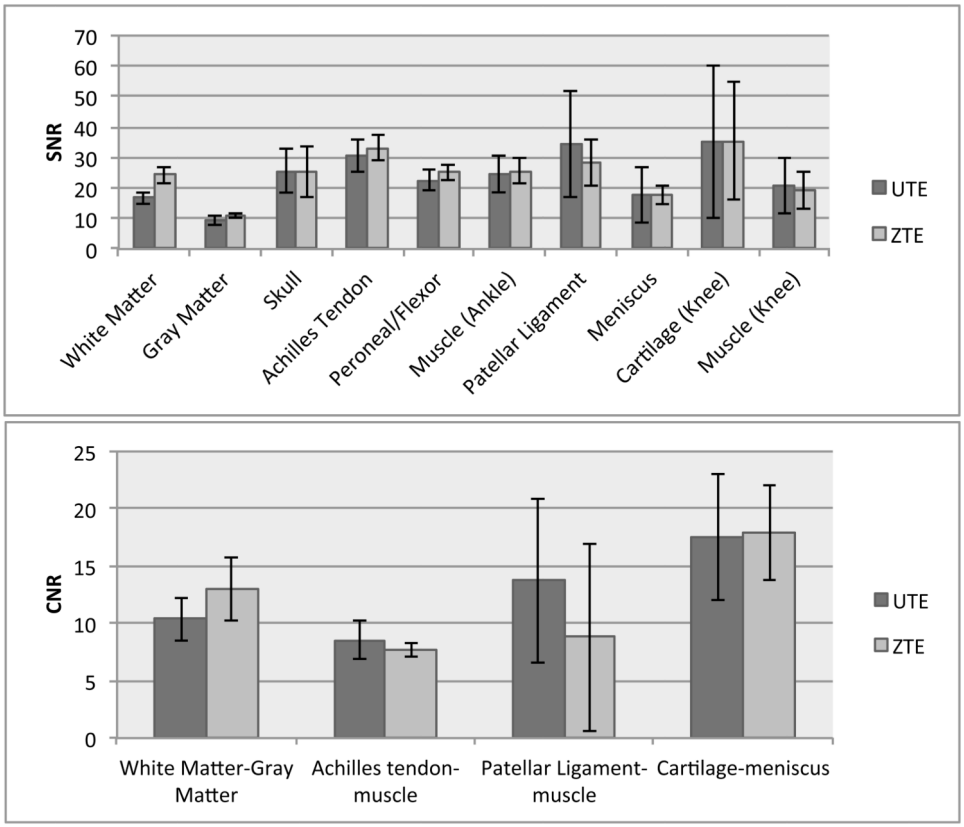

Figure 7.

SNR and CNR comparison of different tissue types between the ZTE and UTE images in the brain (N=5), ankle (N=5) and knee (N=3). There was no statistically significant difference between ZTE and UTE SNR ($p > 0.05$) for all tissues shown except for White Matter ($p < 0.05$). There was no statistically significant difference between the ZTE and UTE CNRs we examined ($p > 0.05$).

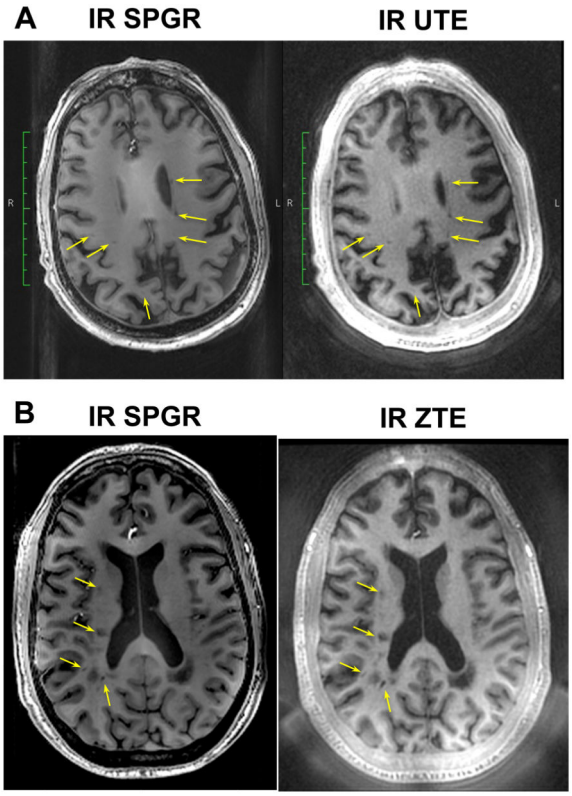

Figure 8.

In vivo brain imaging results in multiple sclerosis patients. The IR SPGR images were acquired at 1 mm isotropic resolution, while the IR UTE and ZTE were acquired at 1.1 mm isotropic resolution with fat-suppression pulses and IR preparation (same parameters as the volunteer images, e.g. in Fig. 3). The UTE and ZTE images clearly depict suspicious lesions (arrows).

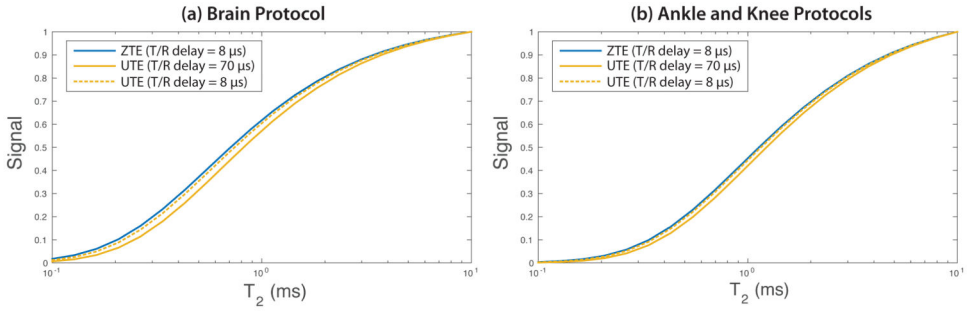

Figure 9.

Theoretical SNR of the UTE and ZTE sequences used in this study with transmit/receive switching delays ("T/R delay") of 70 μs (UTE) and 8 μs (ZTE), as well for an optimized UTE sequence with 8 μs delay. This point spread function simulation accounts for differences due to T2 relaxation during this delay and the readout. In the sub-millisecond T2 regime, there are a larger expected ZTE signals compared to the UTE sequence used in this study, but this expected increase becomes much small with an optimized UTE sequence.

Table 1

Experimental Parameters of the UTE and ZTE pulse sequences. The ranges of UTE parameters correspond to changes required for peripheral nerve stimulation limitations.

	Head		**Ankle**		**Knee**	
	UTE	***ZTE***	***UTE***	***ZTE***	***UTE***	***ZTE***
resolution (isotropic)	1.1 mm		0.7 mm		0.8 mm	
FOV (isotropic)	21.2 cm		22.4 cm		25.6 cm	
Receiver bandwidth	±125 kHz		±125 kHz		±125 kHz	
Samples per readout	192		320		320	
Readout duration	0.768 ms		1.28 ms		1.28 ms	
Readout ramp duration	76 μs	-	68 μs	-	60 μs	-
Flip angle	4°		4°		4°	
RF coil	32-channel Head Coil		32-channel Head Coil		28-channel Knee Coil	
Fat Saturation	Every 128 projections		Every 32 projections		Every 32 projections	
Other Contrast Preparation	adiabatic IR prep		-		-	
ΔT	78 μs	16 μs	76 μs	16 μs	80 μs	20 μs
RF duration	16 μs		12 μs		20 μs	
TR	1.4 – 1.8 ms	1.1 ms	1.9 – 2.2 ms	1.7 ms	1.9 – 2.2 ms	1.7 ms
Total Projections	36,864	37,632	102,400	104,000	102,400	104,000
Scan time	3:30 – 3:42	5:00	3:39 – 4:05	4:30	3:41 – 4:03	4:30

Table 2

Summary of the comparison between the UTE and ZTE methods.

ZTE	UTE
Visualization of ultrashort-T2 components	
Contrast with RF preparation pulses	
Isotropic ringing/blurring off-resonance artifacts	
Shortest possible TE and shorter TR	Variable and multiple TEs
Limitations on FOV/flip angle/readout	Very flexible FOV/flip angles/readout
3D volume	2D, 3D volume, 3D slab
Minimal gradient switching and silent	Very sensitive to gradient fidelity
Need to fill center of k-space	